International Journal of Heat and Mass Transfer 121 (2018) 137–152

Contents lists available at ScienceDirect

International Journal of Heat and Mass Transfer

journal homepage: www.elsevier.com/locate/ijhmt

Dependence of submerged jet heat transfer on nozzle length

Barak Kashi, Herman D. Haustein *

School of Mech. Eng., Tel Aviv University, Tel Aviv, Israel

ARTICLE INFO

Article history:
Received 13 September 2017
Received in revised form 29 November 2017
Accepted 14 December 2017
Available online 5 January 2018

ABSTRACT

In this work the influence of nozzle length in submerged jet impingement heat transfer was studied by validated direct numerical simulations, in the laminar flow regime. With the purpose of examining the entire range of nozzle lengths and $500 \leqslant Re \leqslant 2000$, other effects were reduced by setting a low nozzle-to-heater spacing ($H/D = 3$) and ideal, undisturbed inlet conditions. While developing pipe-flow is well-known, this parametric study characterized in detail short and intermediate nozzle flow regimes, affected by a separation bubble at the sharp-edged inlet. It is found that the maximal (centerline) jet velocity first decreases with increasing effective nozzle length, $Z = L/(D \cdot Re)$, to a minimum at $Z^* \approx 0.0015$, beyond which it increases as in developing pipe-flow. For $Z < Z^*$ two physical regimes are found: while the plane of the vena-contracta is outside the nozzle ($L/D \leqslant 0.6$) the maximal centerline velocity occurs there, rather than at the nozzle exit-plane; whereas in the intermediate range, $0.6 \leqslant L/D$ and $Z \leqslant 0.0015$, the centerline velocity scales with the effective nozzle length, Z, and a predictive correlation could be developed for it. As a clear linear dependence of heat transfer on centerline velocity was observed, this predictive correlation could easily be converted into a new stagnation point heat transfer correlation, found to give good agreement over the entire range of nozzle lengths. This correlation provides a practical design tool, especially applicable to micro-jet cooling where constraints correspond with the new model's validity range.

1. Introduction

Increasing heat flux density of modern micro-electronic devices has promoted a transition to liquid-based forced convection cooling. Amongst the most promising cooling methods is direct jet impingement, in which the perpendicular flow in the stagnation zone is associated with very high heat transfer rates. Local heat transfer distribution under a single submerged impinging jet (IJ) has been studied quite extensively [1,2], providing many empirical correlations for the stagnation point and the distribution of Nusselt number (Nu). These correlations were obtained using either orifice-type nozzles where the issuing velocity profile is assumed to resemble a uniform profile (if somewhat contracted), or long pipe-type nozzles, where the issuing velocity profile is approaching the fully developed parabolic shape. The study of the effects of issuing velocity profile on local Nu has to date been very limited. Recently, the authors [3] in a simulation-based comparison between the fully developed profile and a more uniform, 7th-power issuing profile, found that the stagnation point heat transfer was roughly 60% higher than for the latter. Follow-up studies showed the relaxation of a fully developed velocity profile during flight can cause up to a twofold change in heat transfer [4,52]. Therefore, all aspect which influence the impinging velocity profile, are of importance. While traditionally, the nozzle-to-heater spacing is examined, inherent nozzle aspects are dealt with much less. Studies which have examined nozzle effects on heat transfer can be classified as follows: nozzle cross-section effects vs. nozzle stream-wise variation. The former relates to nozzles shaped as squares, rectangles, ellipsis, star-shaped, etc. [5–7], whereas the latter deals with the inlet/outlet details, such as chamfering/contouring [8–10], nozzle length [11] and resulting issuing profile. The present study deals with the stream-wise aspects of a sharp-edged circular jet, in the short to intermediate nozzle length range. Therein, the jet contraction due to flow separation occurring upon entering a sharp-edged nozzle becomes much more significant. If the nozzle is short enough the jet emerges still under the influence of the entrance contraction (the vena-contracta), and the effective jet diameter measured at the nozzle outlet is altered [12]. Conversely, if the nozzle is sufficiently long the flow recovers from this entrance effect and begins to develop according to classical pipe-flow development [13]. Thus non-monotonous dependence of issuing velocity on nozzle length is expected in the short-intermediate nozzle range ($L \sim D$ in length), which would also be reflected in the impingement heat transfer.

* Corresponding author.
E-mail address: hermanh@post.tau.ac.il (H.D. Haustein).

https://doi.org/10.1016/j.ijheatmasstransfer.2017.12.064
0017-9310/

Nomenclature

C_d	discharge coefficient [–]
C_F	flow coefficient [–]
D	nozzle diameter [m]
h	heat convection coefficient [W/m^2-K]
H	nozzle-to-heater spacing [m]
k	fluid thermal conductivity [W/m-K]
L	nozzle length [m]
p	local pressure [Pa]
$\vec{n}$	unit normal vector [–]
r	radial coordinate [m]
T	local temperature [K]
T_{in}	inlet temperature [K]
u	axial velocity [m/s]
u_m	mean axial velocity [m/s]
u_0	centerline velocity at nozzle exit plane [m/s]
U	normalized centerline velocity, $U = u/u_m$
U^*	normalized centerline velocity at Z^*
U^{**}	normalized centerline velocity at $Z = 0$
y	axial coordinate, measured from the heater [m]
z	axial coordinate, measured from the nozzle entrance plane [m]
Z	Non-dimensional nozzle length, $Z = L/(D \cdot Re)$
Z^*	non-dimensional nozzle length where U is minimal
$\vec{t}$	unit tangential vector [–]
$\dot{q}''$	heat flux [W/m^2]
T	local temperature [K]
Nu	Nusselt number, based on nozzle diameter [–], $Nu = h \cdot D/k$
Pr	Prandtl number [–], $Pr = \nu/\alpha$
Re	Reynolds number, based on nozzle diameter [-], $Re = u \cdot D/\nu$

Greek symbols

α	thermal diffusivity [m^2/s]
η	nozzle shape factor [–]
ν	kinematic viscosity [m^2/s]
ρ	density [kg/m^3]

These intermediate nozzle lengths are the focus of this study, as it is motivated by heat transfer under micro-scale jet arrays. In macro-scale arrays the jets typically issue from perforated plates with nozzle lengths spanning 0.3–6 diameters [14–19]. For micro-jet arrays, structural and fabrication considerations generally raises the minimum realizable length to diameter ratios [20–22] despite the associated higher pumping costs. In addition, the limitations on pumping power generally restricts jet Reynolds numbers (*Re*, based on nozzle diameter) to the laminar range, as seen in previous experimental studies: Reynolds numbers examined in micro-jets experiments, show a trend of decreasing *Re* with decreasing nozzle diameter, demonstrating relevance of laminar flows to jet arrays in the micro-scale [22,23,21,20,24–27], as shown in Fig. 1. At such *Re* and with nozzle lengths characteristically of the order of several diameters, the emerging flow velocity profile can be expected to be neither uniform-like nor parabolic, but somewhere in between these two extremes and not yet predictable.

The study of the effects of issuing velocity profile on local *Nu* has to date been very limited. Following previous studies by one of the authors [3,4], a novel heat transfer correlation (Eq. (1)) incorporating the evolution of an initially fully-developed profile during flight was developed [28], where the dependence on *Pr* is given in Eq. (2) taken from Ref. [29]. Comparing this recent correlation with an established empirical one (Eq. (3)), obtained using a nozzle length of 35 diameters – not necessarily fully-developed without considering flight evolution, at $Re = 1000$ and $Pr = 4.5$ the former gives $Nu = 86.4$, whereas the latter is significantly lower at

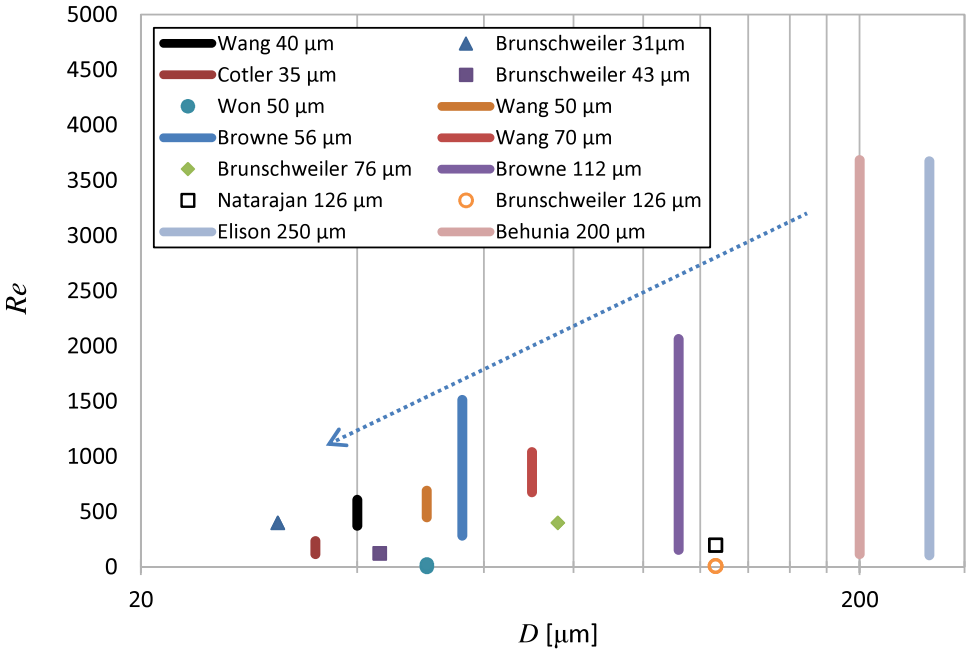

Fig. 1. Reynolds numbers ranges examined in micro-jets experiments shows a trend of decreasing maximal Reynolds number with decreasing nozzle diameter and relevance of laminar flows.

$Nu = 63.2$ [30]. This demonstrates the need to address the specific impinging velocity profile, which is strongly related to nozzle length (flow development).

$$\frac{Nu_0}{Re^{0.5}G(Pr)} = 2.31\exp\left(-10.2\frac{H/D}{Re}\right) + 0.51 \quad (1)$$

$$G(Pr) = \begin{cases} \frac{\sqrt{2Pr/\pi}}{1+0.804552\sqrt{2Pr/\pi}}, & Pr \leqslant 0.15 \\ 0.53898Pr^{0.4}, & 0.15 \leqslant Pr \leqslant 3 \\ 0.60105Pr^{\frac{1}{3}} - 0.050848, & Pr > 3 \end{cases} \quad (2)$$

$$Nu_0 = 1.21Pr^{1/3}Re^{0.5} \quad (3)$$

In fact, only very few heat transfer correlations have incorporated the *nozzle length*. One of these is the work of [11] who considered the stagnation point *Nu* (Eq. (4), and its dependence on nozzle length and effective heater diameter D_e). However, this correlation is only valid for nominally turbulent flows, $Re > 4000$, where the velocity profile development is rather different than in the laminar flow considered here.

$$Nu_0 = 1.427Pr^{0.444}Re^{0.496}(L/D)^{-0.058}(D_e/D)^{-0.272} \quad (4)$$

Some heat transfer studies have introduced nozzle length and shape related effects, in a *global* way through the flow or discharge coefficient. Meola [31] incorporated the flow coefficient, $C_F = C_d/\eta$, in a correlation for average heat transfer in arrays of IJ (Eq. (5)), where A_r is the jet to heater area ratio, C_d is the discharge coefficient and η is a factor related to nozzle shape. This coefficient is intended to account for jet contraction and the corresponding increase in issuing *Re*, though values for η in the literature are scarce. Although $\eta = 1$ ($C_F = C_d$) can be assumed for straight nozzles, to the best of our knowledge it has still not been shown in detail how jet contraction, the corresponding issuing velocity profile and resulting heat transfer, depend on nozzle length. While values and correlations

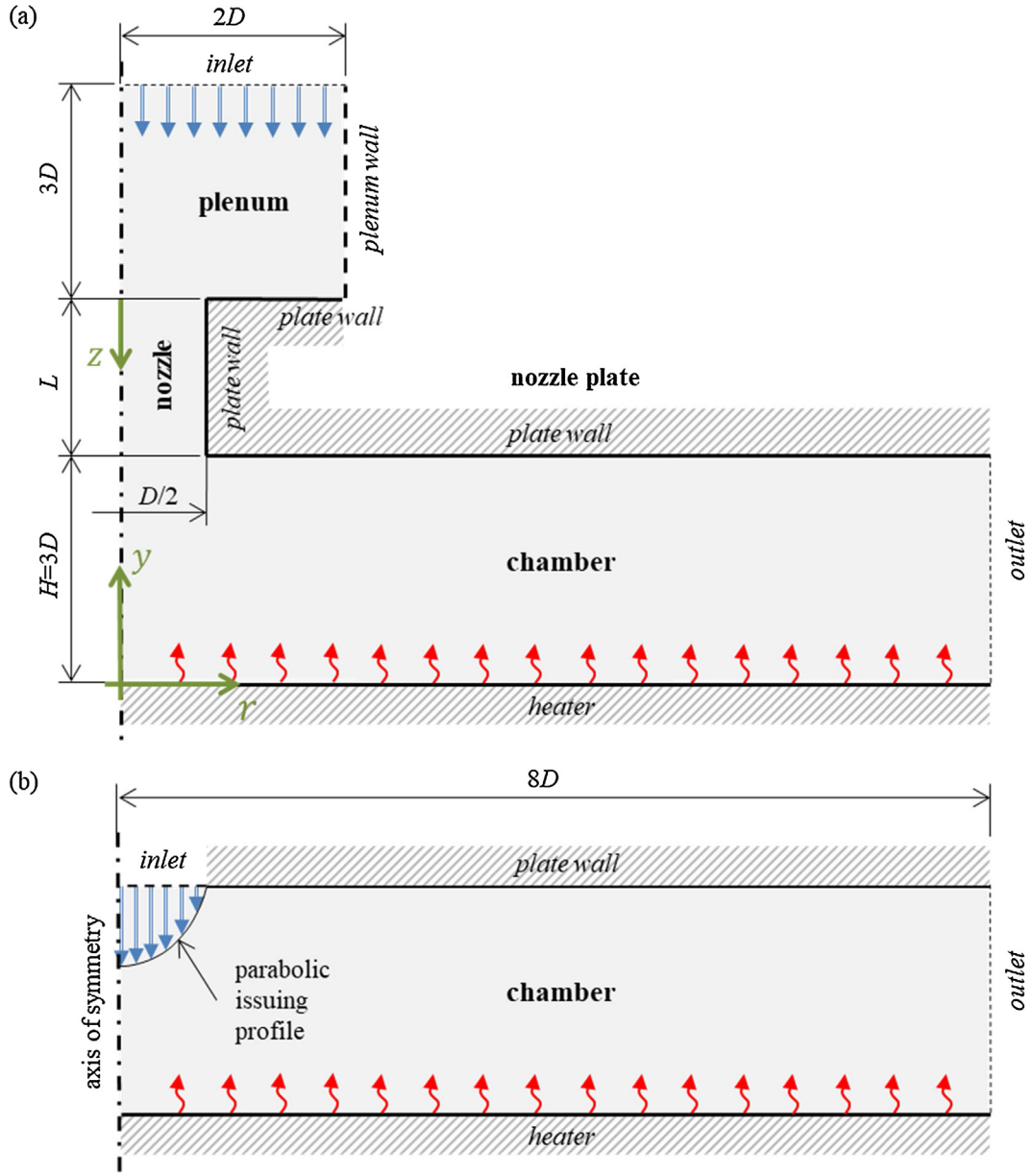

Fig. 2. The model geometry: (a) the case of finite length nozzle, consisting of a plenum, a nozzle and a chamber. (b) The case of the fully developed inlet velocity profile, where the plenum and nozzle are removed, and a parabolic profile is imposed at the inlet.

for C_d can be found for flow restricting orifices inside larger pipes [32,33], these do not consistently agree with reported results from micro IJ arrays [34,18]. For example, at $Re = 2000$, $L/D = 2$, where $C_d = 0.44$ according to the model by Jankowski et al. [33], vs. a value of 0.81 from Fabbri and Dhir [34]. This discrepancy may be related to the proximity of the impingement surface which is absent in the case of an orifice within a pipe, or the restriction of the larger pipe. Even the mentioned impingement-specific IJ-array correlations are restricted to a limited range of conditions.

$$\overline{Nu} = 0.3Pr^{0.42}Re_d^{0.68}C_F^{0.56}(H/D)^{-0.3}A_r^{0.15} \tag{5}$$

In light of the knowledge gap described above, the present work lays the foundation for a detailed description of jet profiles that issue from short and intermediate nozzles, and their effects on local heat transfer in a laminar submerged IJ. The conditions examined here were chosen so as to minimize additional effects on the impingement centerline velocity, thereby the study was limited to a specific low nozzle-to-heater spacing and ideal, undisturbed inlet conditions. An extensive literature review of heat transfer under a single submerged jet, conducted within a preliminary study [35], revealed very few correlations for an orifice ($L < D$) and none for short-to-intermediate nozzles ($L \sim D$). This gap is thereby addressed in a *fundamental* and *extensive* manner, through detailed unsteady numerical simulations. Therein, the dominant physical regimes are characterized and are formulated as novel flow and heat transfer correlations.

2. Methods

In this work two configurations of confined axisymmetric impinging jets were modeled. The first (Fig. 2a), denoted *nozzle,* is a case of a jet emerging from a nozzle of finite length, where the issuing velocity profile depends on the nozzle length, and therefore the model includes the nozzle itself in addition to the chamber that contains the impinged surface denoted *heater*. Moreover, in order to avoid any constraint on the velocity profile in the

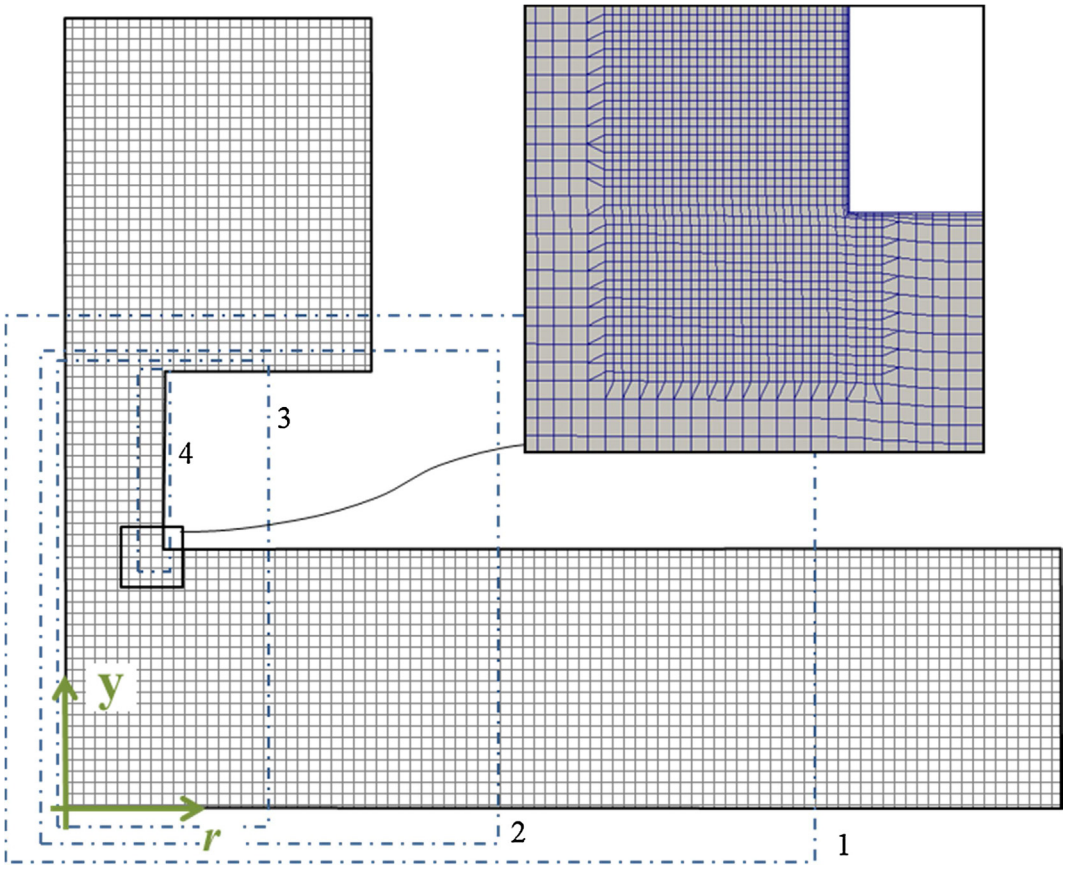

Fig. 3. The mesh with four levels of cell refinement by method of cell splitting.

Table 1
Boundary conditions.

	Inlet	Outlet	Plate wall	Heater	Plenum wall
$\vec{u}$	Finite nozzle: $\vec{u} = (0, -U)$ Fully developed: $\vec{u} = (0, -U(1 - 4r^2/D^2))$	$\begin{cases} \frac{\partial(\vec{u}\cdot\vec{n})}{\partial\vec{n}} = 0, & \text{outflow} \\ \vec{u} = \vec{0}, & \text{inflow} \end{cases}$ (inlet/outlet BC)	$\vec{u} = \vec{0}$	$\vec{u} = \vec{0}$	$\begin{cases} \vec{u}\cdot\vec{n} = 0 \\ \frac{\partial(\vec{u}\cdot\vec{t})}{\partial\vec{n}} = 0 \end{cases}$ (symmetry or slip-wall BC)
p	$\frac{\partial p}{\partial n} = 0$	$p = 0$	$\frac{\partial p}{\partial n} = 0$	$\frac{\partial p}{\partial n} = 0$	$\frac{\partial p}{\partial n} = 0$
T	$T = T_{in}$	$\frac{\partial T}{\partial n} = 0$	$\frac{\partial T}{\partial n} = 0$	$k\frac{\partial T}{\partial n} = \dot{q}''$	$\frac{\partial T}{\partial n} = 0$

entrance to the nozzle, a supply volume denoted *plenum* is modeled as well. This case is utilized with various nozzle lengths in order to study the dependence of heat transfer on the nozzle length at various *Re*.

The second (Fig. 2b), denoted *pipe*, is a case of a jet emerging from a sufficiently long nozzle, such that the issuing velocity profile is fully-developed. In this case a parabolic emerging velocity profile is imposed, and the nozzle itself is not modeled. This model is used both for validating the simulations, as it is a known limiting case, and for establishing the limiting case values in the correlations developed for the hydrodynamics of jet flight and the heat transfer in the impingement zone.

Since the issuing velocity profile depends on both the nozzle Reynolds number and the nozzle length, three values of Reynolds number were simulated and for each of them a series of nozzle lengths were modeled. The values of Reynolds number considered in this work were 500, 1000 and 2000, as they are spread across the range of Reynolds numbers typical to impinging jets in the micro scale, as explained in the introduction section (Fig. 1). For each Reynolds number 11 nozzle lengths were modeled including the asymptotic *pipe* case. In all the simulations mentioned above, the thermo-physical material properties corresponded to water at 40 °C ($Pr = 4.5$) set at the inlet. However, an additional series of simulations with 9 different nozzle lengths was performed for $Pr = 6.15$ at $Re = 2000$, and for validation of Eq. (2) two more simulations at $Re = 500$ for $Pr = 0.5$ and $Pr = 50$ were conducted. The separation distance between the nozzle exit plane and the *heater* was fixed at $H/D = 3$ throughout the study although it was previously shown that profile relaxation during flight affects the arriving profile at the impinged surface [28]. However, in the context of arrays of micro-jets, compactness considerations make the relevant separation distances are relatively small, and therefore these effects are expected to be small.

The computational domain was meshed using two meshing applications included in the OpenFOAM package [51]. Initially, a base hexahedral mesh was created using the "blockMesh" application with uniform cell size everywhere except 20 layers of thin cells adjacent to the *heater* boundary with an inter-cell growth size of 1.034 (Fig. 3). Then the application "snappyHexMesh" was used to locally refine the base mesh by adding three layers of thin cells near the *plate wall* and by splitting cells in 4 consecutive levels, as described in Fig. 3. The first cell thickness adjacent to the *heater* was determined using the analytical solution for stagnation flow, where the velocity gradient is given in tabulated form, in order to capture the velocity gradient within 1% accuracy. The resulting cell thickness was 0.21 m for $Re = 2000$ and $D = 0.001$ m after

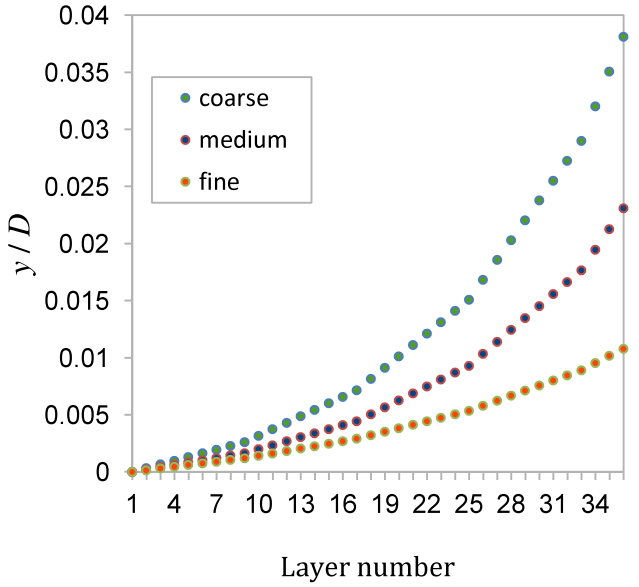

Fig. 4. Growth of cell thickness near the heater for the three meshes.

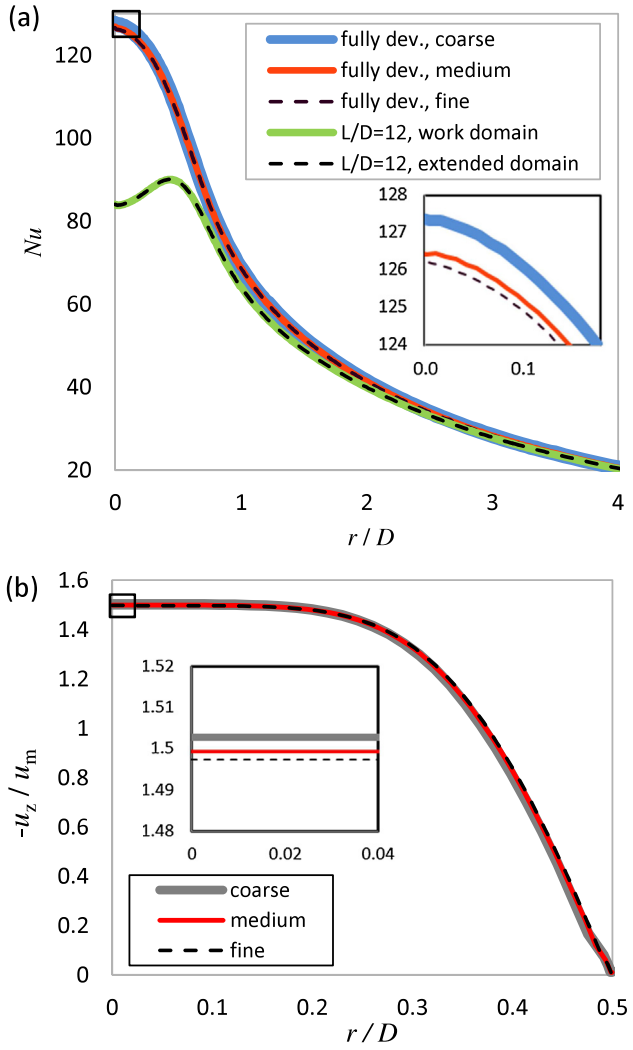

Fig. 5. Mesh and domain independence at $Re = 2000$: (a) local *Nu* for the fully-developed case and for $L/D = 12$ and (b) issuing velocity profile for $L/D = 12$.

Table 2
Discretization errors.

Parameters of GCI Procedure [37]	$\phi = Nu_{(r=0)}$ Fully developed case	$\phi = Nu_{(r=2D)}$ Fully developed case	$\phi = u_0$ Finite nozzle case
N_1, N_2, N_3	129,510; 57,432; 23,725		59,872; 127,355; 271,424
r_{21}	1.50		2.13
r_{32}	1.56		2.13
ϕ_1	126.6	41.220	1.497
ϕ_2	126.9	41.239	1.499
ϕ_3	127.7	41.493	1.503
P	2.275	9.390	10.390
ϕ_{ext}^{21}	126.40	41.22	1.50
e_a^{21}	0.24%	0.047%	0.155%
e_{ext}^{21}	0.16%	0.001%	0.0001%
GCI_{fine}^{21}	0.20%	0.001%	0.0001%
GCI_{coarse}^{21}	0.49%	0.060%	0.1933%
GCI_{fine}^{32}	0.46%	0.012%	0.0001%

the local refinement stage. The boundary conditions (BC) applied are given in Table 1 and listed as follows: no-slip at the *wall* and *heater* boundaries; constant zero pressure at the *outlet* boundary, with the complementary velocity BC that allows inflow (as used in [3]) – as occurs when a vortex exits the domain; uniform inlet velocity BC at the *inlet* of the *nozzle* case; parabolic velocity profile at the inlet of the *pipe* case; symmetry at the *plenum wall* boundary; and a uniform heat flux of 126 kW/m^2 (constant temperature gradient) at the *heater* boundary, a value relevant to microelectronics. Under the assumption of constant properties, it is well-known that the single phase heat transfer coefficient should be independent of heat-flux level. This was verified through a comparison, the fully-developed jet case at $Re = 1000$ was solved once with the mentioned heat flux and once with less than half of it ($\dot{q}'' = 50$ kW/m^2). In the comparison the radial heat transfer distributions could not be distinguished from each other, and hence this value has no influence on the dimensionless form of the results.

The unsteady incompressible Navier-Stokes equations were solved directly for this primarily laminar flow using the open source CFD package OpenFOAM employing the finite volume method. The pressure and velocity fields were solved by the "pimpleFoam" solver employing the PISO scheme and adaptive time stepping for constant Courant number equal to 0.5. The convergence criteria in each time step were residual's values smaller than 10^{-8} and 10^{-6} for the pressure and velocity fields, respectively. The temperature field was resolved by solving the transport equation assuming the temperature is a passive scalar (i.e. with only one way coupling), which is valid for lower heat fluxes, where no significant thermally-driven property change occurs. Although in many high-power/low-flow applications significant thermal variation near the heater can be expected to cause some property

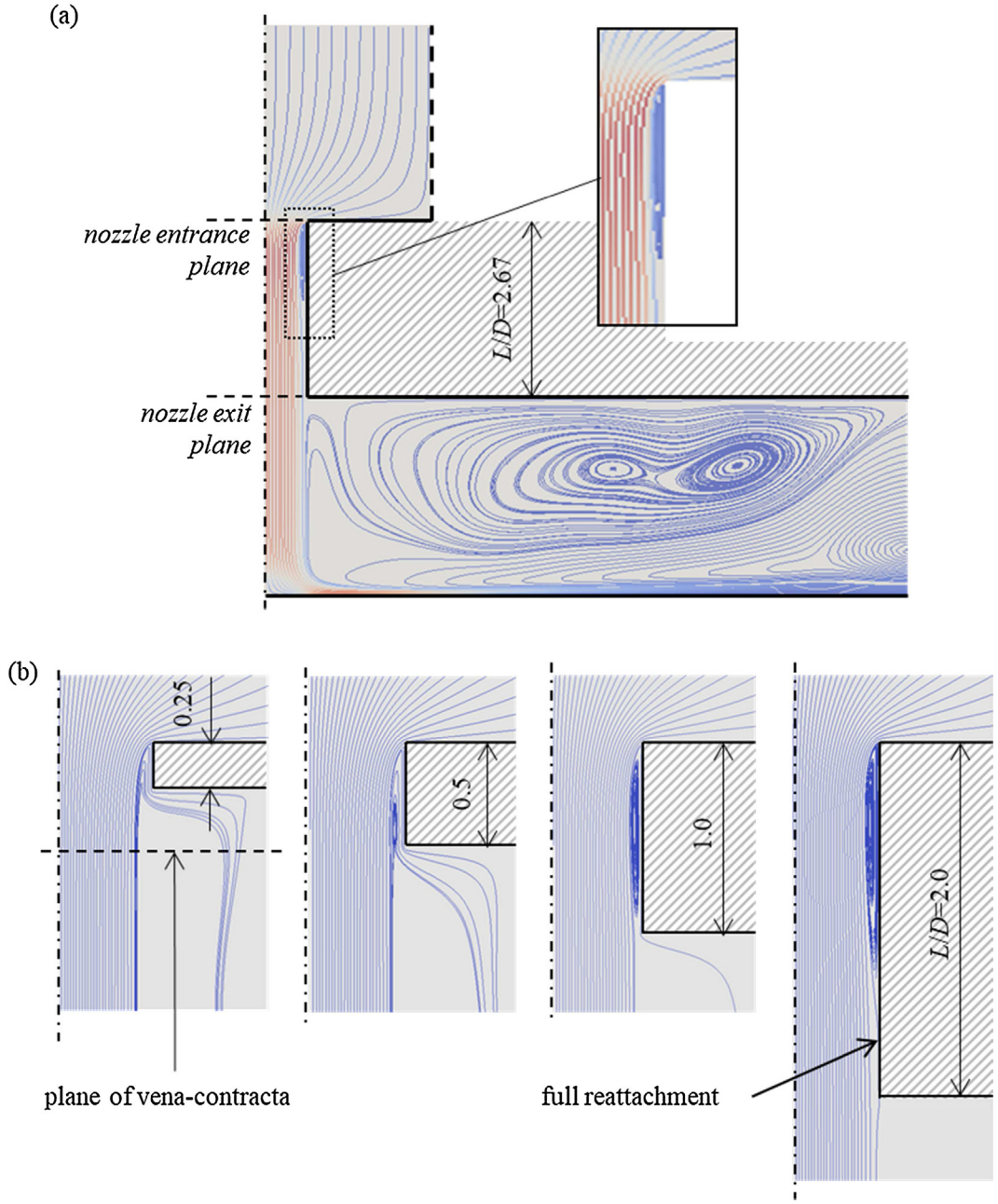

Fig. 6. Streamlines at *Re* = 2000: (a) colored by velocity magnitude shown in the entire domain for the case of L/D = 2.6 and (b) nozzle zone with separation bubble for the cases L/D = 0.25, 0.5, 1 and 2.

changes, the present study focuses on describing the dominant convection, laying a foundation which can subsequently be further developed, as is often done.

The non-dimensional heat transfer coefficient was calculated as in Eq. (6), where T is the local temperature along the *heater* boundary, $\vec{n}$ is a unit vector normal to that boundary, $\frac{\partial T}{\partial \vec{n}}$ is the imposed temperature gradient there, D is the nozzle diameter, and T_{in} is the fluid temperature at the inlet. Convergence criterion in each time step was residual's values smaller than 10^{-6}.

$$Nu = \frac{\left.\frac{\partial T}{\partial \vec{n}}\right|_{y=0} D}{T - T_{in}} \tag{6}$$

Each simulation was run until all initial transients and vortices exited the domain or settled and a steady-state was observed (Nu fluctuations below 1% for $0 \leqslant r/D \leqslant 4$). The required time depended on Reynolds number, and was between 200 and 1600 ms.

Mesh independence tests were performed at $Re = 2000$ with the *pipe* and *nozzle* ($L/D = 12$) cases. Each model was solved with an initial "coarse" mesh and two consecutively refined meshes - "medium" and "fine". In each refinement the total cell count was at least doubled. As shown by Rohlfs [3], a very fine grid is required near the heated wall in order to correctly capture the thermal boundary layer. Fig. 4 shows the growth of cell thickness near the heater for the three meshes. Fig. 5a shows the comparison of the heat transfer distribution on the *heater for both cases*, whereas Fig. 5b shows the comparison of the issuing velocity profiles at the nozzle exit plane for the *nozzle* case. Meshes were deemed size-independent when differences in results were smaller than 1.5%. The following simulations were performed with the "medium" meshes consisting of 57,432 cells for the *pipe* case, and depending on the nozzle length between 61,922 and 163,214 cells, in the *nozzle* case.

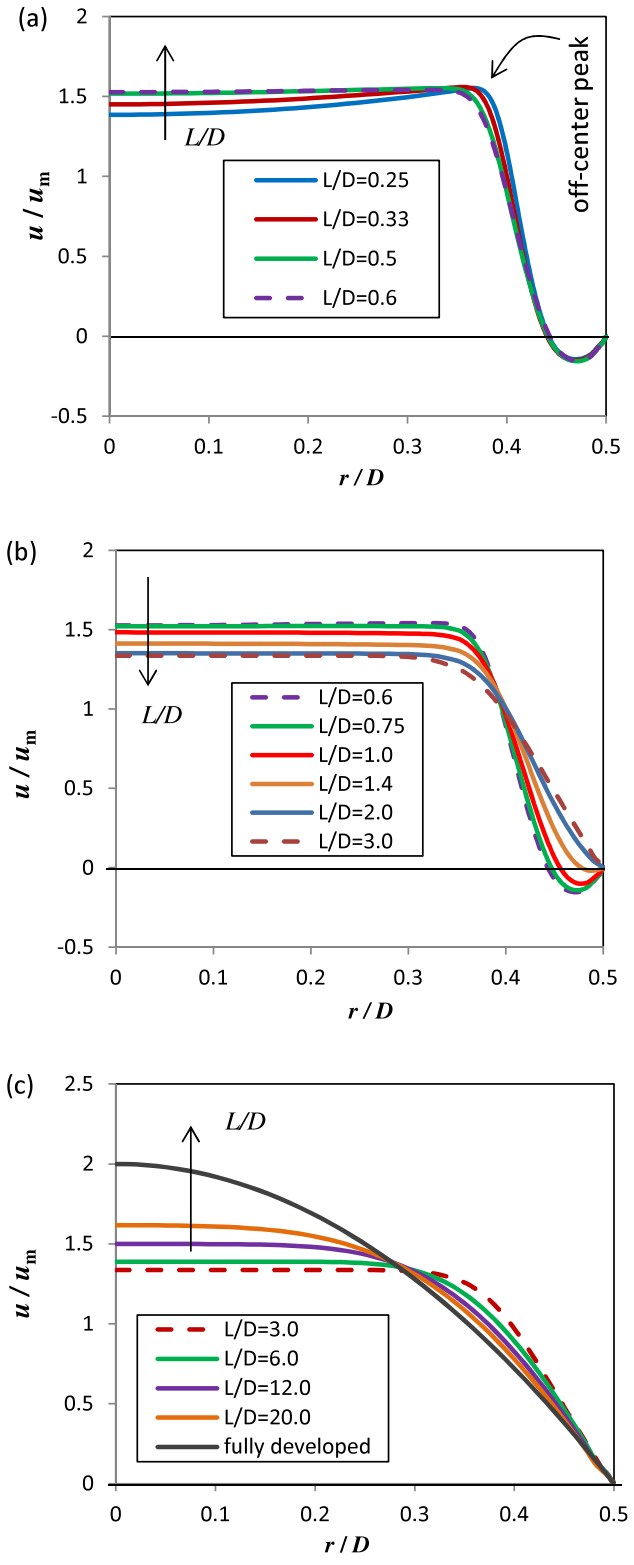

Fig. 7. Velocity profiles at the nozzle exit plane for $Re = 2000$, featuring three flow regimes: (a) peak convergence, (b) divergence, and (c) development.

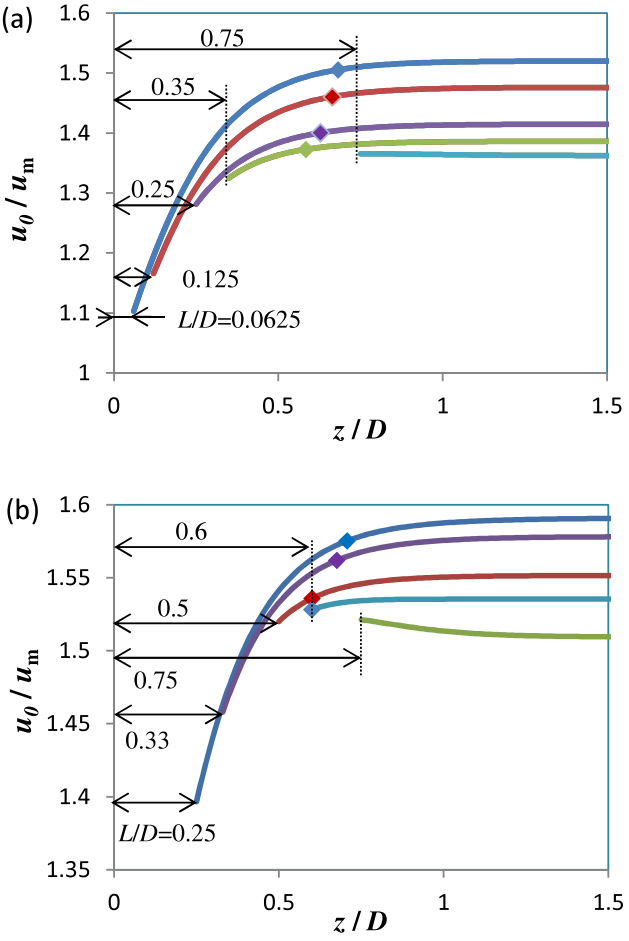

Fig. 8. Evolution of normalized centerline velocity as a function of normalized nozzle length for: (a) $Re = 500$ and (b) $Re = 2000$. The diamond shaped markers indicate where velocity reached 99% of its maximum, and the arrows represent the nozzle lengths.

The accuracy of the numerical results was estimated using the grid convergence index (GCI), which is a procedure based on the Richardson extrapolation, as detailed in Refs. [36,37]. The convergence was evaluated by the parameters listed in Table 2, at = 2000, wherein the Nusselt number at $r = 0$ and $r = 2D$ and the centerline velocity at the nozzle exit plane were used as variables for the GCI procedure, and the discretization error for the "medium" mesh was 0.5%.

A domain size study was performed as well, where the distances from the *inlet* to the nozzle entrance, the centerline to the *plenum wall* and the centerline to the *outlet* were all doubled. Similar comparisons as in the mesh study showed that the various domains generated differences smaller than 1% in results (see Fig. 5a).

3. Results

3.1. Issuing profile and flight velocity

The results of the simulations were used to study the nozzle hydrodynamics, and in particular, the separation bubble that is formed at the entrance of the nozzle.

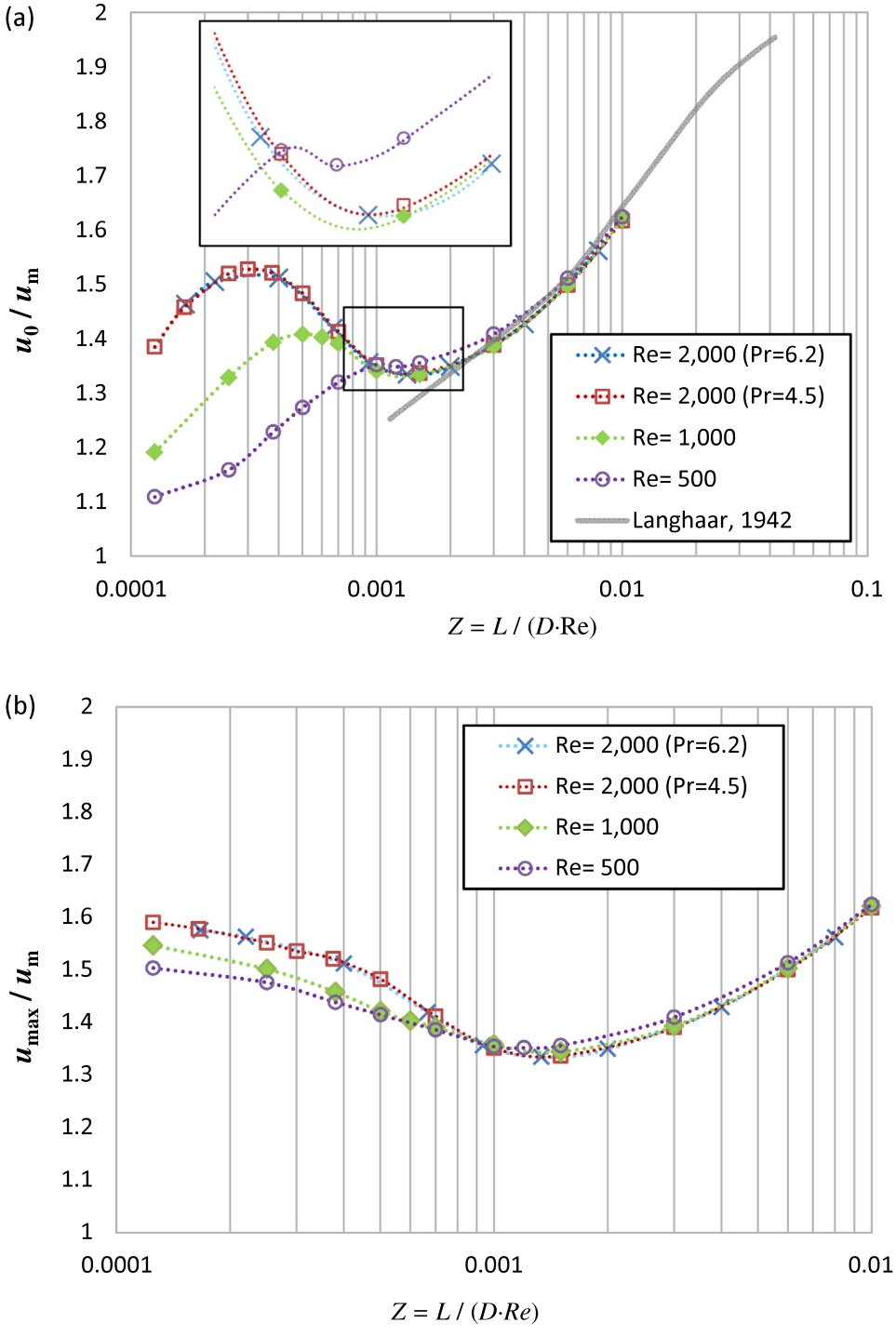

Fig. 9. Dependence of normalized centerline velocity on effective nozzle length: (a) at nozzle exit plane with comparison to a developing pipe flow analytical solution [13] and (b) maximum during flight.

Fig. 6a shows streamlines of the entire flow field for $Re = 2000$ and $L/D = 2.67$ with indication of the nozzle entrance and exit planes. The flow enters the plenum, and then converges in order to enter the nozzle. The sharp edge of the nozzle entrance deflects the flow towards the centerline, and thus a recirculation zone is formed adjacent to the nozzle wall, the dynamics of which depend on flow rate and nozzle length.

Fig. 6b shows close-up views of the recirculation zone for various nozzle lengths at $Re = 2000$, following known flow patterns [12]. In the case of the shortest nozzle ($L/D = 0.25$) the jet continues to converge beyond the nozzle exit plane, and the vena-contracta is defined at its narrowest cross-section where it ceases to converge [38]. At $L/D = 0.5$, the vena-contracta is still apparent downstream of the nozzle exit, whereas at $L/D = 1$ the main-flow diverges towards the beginning of reattachment. By $L/D = 2$ full reattachment is obtained and the main-flow aligns with the nozzle wall.

The jet travels towards the impinged surface at a high velocity, entraining surrounding stationary fluid, and forming a pair of large scale low-velocity vortices that span across the chamber.

At the impingement zone the flow is deflected radially towards the outlet, where a wall jet is formed with a boundary layer growing in stream-wise direction.

The issuing velocity profile, at the nozzle exit plane, for all nozzle lengths at $Re = 2000$ is shown in Fig. 7a–c. Initially, for the shortest nozzle, the velocity profile exhibits an off-center peak where the velocity is maximal, and a reduced centerline velocity. However, as the nozzle length is extended, this phenomenon diminishes such that the centerline velocity becomes the highest in the entire profile (Fig. 7a), at around $L/D = 0.6$.

Fig. 7b shows velocity profiles beyond the narrowest cross-section, approaching flow reattachment. Here the near-wall reverse flow reduces as the nozzle length is extended, until its disappearance at full reattachment, occurring near $L/D = 2$ in this case.

Beyond full reattachment, as the nozzle length is increased further, the velocity profile begins to develop as in nominal pipe flow: with increasing centerline velocity converging towards the well-known parabolic profile (Fig. 7c).

Fig. 8a and b for $Re = 500$ and $Re = 2000$, respectively, show the evolution of the centerline velocity during flight, revealing a phenomenon that is hereby characterized in greater detail than before. The centerline velocity of the profile issuing from the *shorter* nozzles continues to increase during flight, in spite of the viscous shear forces of the stagnant fluid acting on the jet. It is seen that the shorter the nozzle, the greater the extra-nozzle acceleration, whereas nozzle lengths around $L/D = 0.75$ have the familiar monotonously decaying centerline velocity [3,4]. The diamond markers indicate where the centerline velocities obtain 99% of their respective maximal values during flight and all seem to fall within the range of 0.5–0.7 nozzle diameters from the nozzle entrance plane. These positions closely coincide with the position of the vena-contracta shown in Fig. 6b for $Re = 2000$. However, more accurate determination of the stream-wise position where the jet reaches its narrowest section requires a higher mesh resolution, than that used here, and due to the associated increased computational cost it is left for a future study.

The nozzle lengths that exhibit this extra-nozzle centerline acceleration correspond to the issuing profiles that contain an off-center peak in the velocity profile shown in Fig. 7a. Therefore this acceleration can be attributed to the main-flow convergence (while at the wall the flow separates), during which there is the peak-relaxation and the recovery of a profile with the peak velocity at the jet center. This peak relaxation and centerline acceleration is here described in detail for the first time. This flow regime is denoted the *convergence* regime that precedes the *divergence* (Fig. 7b) and flow *development* regimes (Fig. 7c).

Fig. 9 shows the centerline velocity's dependence on the effective nozzle length, $Z = L/(D \cdot Re)$, a well-known scaling for pipe-flows [39], for all finite nozzle lengths and all *Re*. Fig. 9a shows the centerline velocities at the nozzle exit plane, showing that with this scaling all three curves coincide for $Z \geqslant 0.0015$, within the aforementioned *development* regime. In this range, good agreement with previous theoretical solutions for developing pipe flows is observed [13]. Starting from the shortest nozzle, the centerline velocity increases with increasing nozzle length since the vena contracta is still downstream from the nozzle, and the velocity at its exit plane is still not maximal. As reattachment begins the jet diameter at the exit plane begins to increase, and the velocity at the exit-plane continues to decreases with nozzle extension until full reattachment occurs. From that point on, the profile continues to develop as in nominal developing pipe-flow.

Since it was found that the centerline velocity accelerates outside the nozzle in the *convergence* regime, and knowing that the **arriving velocity** of the jet is the important factor in impinging jet's heat transfer [3], Fig. 9b depicts the **maximum** centerline velocity obtained during flight towards the heater as a function of effective nozzle length. Beginning again from the shortest nozzle, the maximal centerline velocity first decreases with increasing nozzle length, until it reaches a minimum at around $Z = 0.0015$, transitions to the *development* regime and begins to increase again. This is very significant, as it shows that for a desired maximal velocity two pathways exist: for instance, if a maximal velocity of around $\boldsymbol{u_0/u_m} = 1.55$ is desired at $Re = 2000$ it can be found either one diameter *downstream* of a short nozzle ($L/D = 0.5$) or directly *at the exit* of one about **30 times longer**! In other words, where nozzle length constrains are important, Fig. 9 sheds light on the preferable configuration to obtain a desired impingement-velocity and consequent heat transfer, shown in the following.

3.2. Correlation for centerline velocity

Considering the trends seen above for the maximal velocity, obtained around the location of the vena- contracta, it may be argued that it could be predicted as the inverse of the flow contraction coefficient for nozzles. Assuming the velocity coefficient is

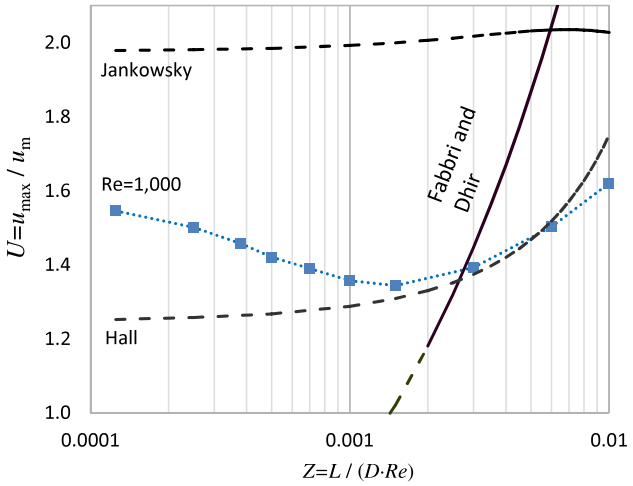

Fig. 10. Comparison of the current normalized centerline velocity with values derived from correlations for the discharge coefficient [32,34,33]. Dashed lines represent extrapolation of the correlations beyond their valid ranges.

close to unity the contraction coefficient roughly equal to the discharge coefficient. Several correlations for the discharge coefficients are available in the literature. Fig. 10 shows a comparison of the prediction of several such correlations for the maximal velocity emerging from a jet. As the figure shows, these correlations present a monotonous trend and values which are not in agreement with the present findings. Therefore, the task of predicting this velocity maximum, $U_{max} = u_{max}/u_m = f(Re, L/D)$, was undertaken.

Starting from the more familiar *development* regime in the present case, a previously obtained nominal pipe-flow development correlation was adapted [40], as per Eq. (7), to account for the existence of a separation bubble at the nozzle inlet:

$$\frac{u_0(Z)}{u_m} = 1.18 + (2 - 1.18)(1 - e^{-\zeta_1(Z+Z_1)}) \tag{7}$$

In the original correlation the values of Z_1 and ζ_1 were -0.002 and 78, respectively. The latter was chosen so that the centerline velocity will reach 99% of its maximum value by $Z = 0.05 \cdot Re$, and the former for obtaining agreement with experimental data at short pipe lengths. However, as the present study includes a separation bubble not considered there, an offset of this development occurs leading to $Z_1 = Z^* = 0.0015$, which gives $\zeta_1 = 71$ in order to satisfy the original requirement, $U_0 = 99\% Umax$ @ $Z = 0.05 \cdot Re$. This implies that for sufficiently long nozzles, $Z_1 \geqslant 0.0015$, the development flow follows the well-known pipe-flow curve, though it begins at a higher velocity than expected due to the presence of the inlet separation bubble. This bubble is associated with rapid acceleration of the main-flow at the inlet during flow-convergence with reduced friction, followed by a more gradual divergence (during the reattachment phase), which still leads to an overall relative increased velocity. Thereby, this separation bubble whose effect

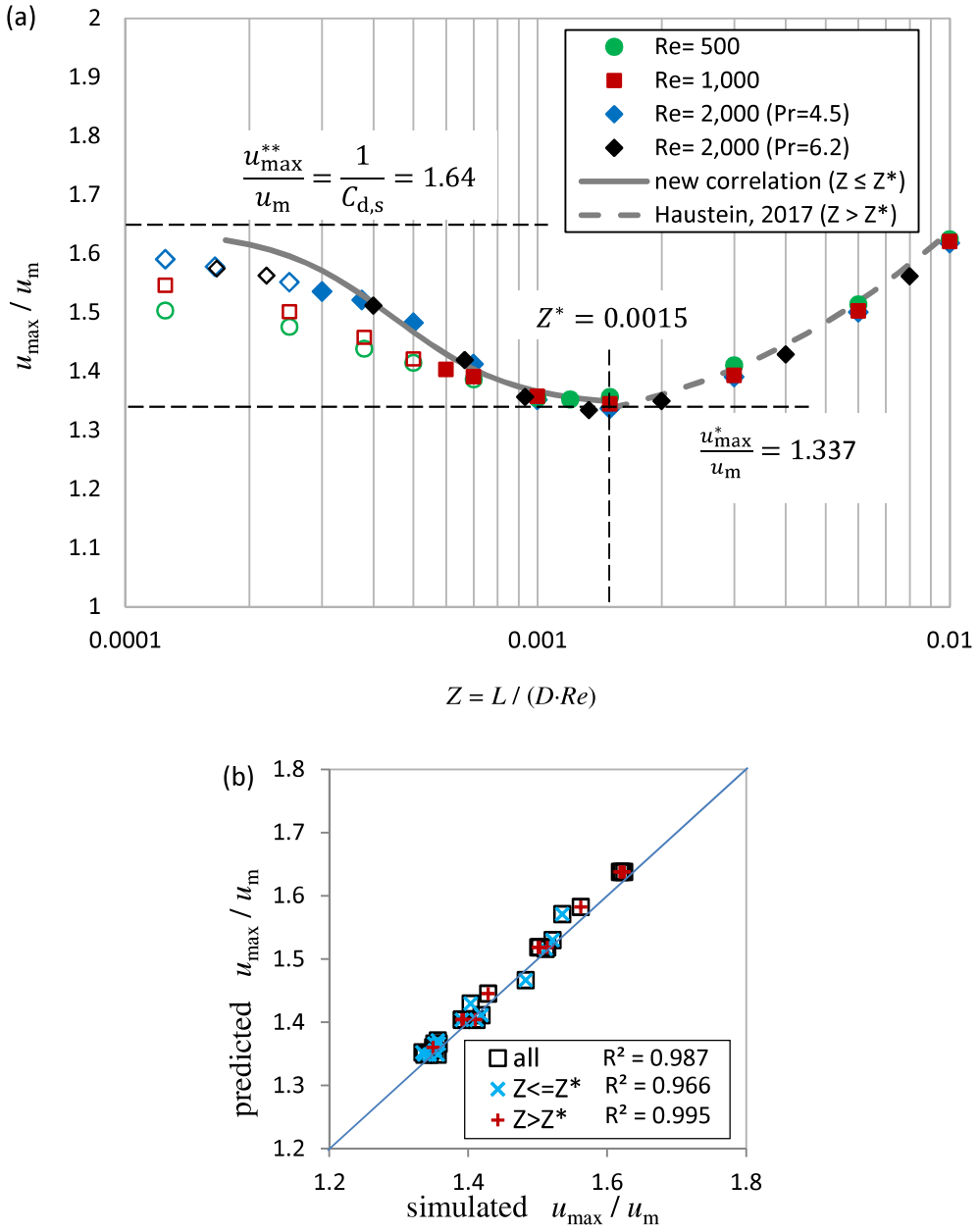

Fig. 11. Evaluation of centerline velocity prediction by the new model: (a) Prediction by Eq. (7) for $Z \geqslant Z^* = 0.0015$ and Eq. (8) below this nozzle length. (b) Evaluation of prediction performance for each equation within the valid range.

ends around $Z^* = 0.0015$ brings the flow to a centerline velocity, which it would have reached in nominal inlet pipe flow within a hydrodynamic length of $Z = 0.005$.

Eq. (7), adapted from a previous study, correlates the data within the *development* regime, $Z \geqslant Z^*$, whereas the present study's primary contribution is providing a tool for dealing with short and intermediate nozzles, in the preceding *convergence* and *divergence* regimes.

In order to capture the transition from the initial regime to the next in a smooth way, a function with an inflection point was employed, as in Eq. (8):

$$U(Z) = \frac{1}{2}(U^{**} + U^*) + \frac{1}{2}(U^{**} - U^*)\tanh\left(\zeta_2 \ln\frac{Z}{Z_{\text{infl}}}\right) \tag{8}$$

This function has to vary smoothly between the maximum value at $Z = 0$ and the minimum value of $U^*_{\max} = 1.337$ derived by substituting Z^* into Eq. (7), where $Z = 0$ represents the limiting case of sharp nozzle ($L/D = 0$). In the sharp nozzle case, the centerline velocity at the plane of vena contracta can be derived from the definition of the contraction coefficient, and Eq. (9) as the relationship between the contraction, velocity and discharge coefficients [31]:

$$C_d = C_v C_c \tag{9}$$

It should be noted that while the value of C_c is equal to unity within 1% for $Re \geqslant 10,000$ [41], experimental results [42] show that this value reduce only slightly at $Re \geqslant 2000$ for small diameter ratios which imply that the contraction coefficient is still close to the discharge coefficient. The value $C_{d,s} = 0.61$ is well established [12,43], and we arrive at $U^{**} = \frac{1}{C_{d,s}} = 1.639$. This leaves two model parameters to be established, $\zeta_2 = 1.5$ and $Z_{\text{infl}} = 0.00045$, which were found from a fit to the current data below Z^*.

As shown in Fig. 9a, the normalized centerline velocity begins to scale with the effective hydraulic length Z, only for $L/D \geqslant 0.6$. Therefore Eq. (8) is valid for $Nu/f(Pr)$ $Z \leqslant 0.0015$, $\frac{L}{D} \geqslant 0.5$ and $500 \leqslant Re \leqslant 2000$. The quality of prediction of numerical results of maximal centerline velocity in the valid range by Eqs. (8) and (7) is shown to be quite good in Fig. 11a. Fig. 11b quantifies the correlation between the numerical results with predicted values, where the coefficient of determination for the new correlation in the range $Z \leqslant 0.0015$ is $R^2 = 0.96$, and for the entire range (with the development regime) $R^2 = 0.98$.

3.3. Heat transfer

For dealing with the heat transfer at the stagnation point ($r = 0$) the temperature field was resolved as a passive scalar in all simulations, which was then used to calculate the heat transfer coefficient on the heater surface.

The first step taken was to validate the dependence of heat transfer on the Prandtl number, suggested in Eq. (2) taken from Ref. [29], as shown in Fig. 12. The figure compares the dimensionless heat transfer normalized by two different Pr dependencies, seeking out the form of $f(Pr)$ which collapses all curves most successfully. As the figure shows, just using the commonly accepted proportion for $Pr > 1$: $Nu \sim Pr^{1/3}$, is less successful than using Eq. (2), with which curves coincide quite well over 2 orders of magnitude (relevant to most engineering fluids – $0.5 < Pr < 50$).

Fig. 13 compares present heat transfer distribution numerical results to the nearest data from the literature. The comparison to previous experimental data of deionized water flow, at $Re = 2497$ and $L/D = 6$ or $Z = 0.0024$ [44], with the present local Nu distribution, $Re = 392$ at $Re = 2000$ and $L/D = 6$, or $Z = 0.003$, shows reasonably good agreement. Nusselt number values are normalized by $Re^{0.5}$ and a function of the Prandtl number in stagnation flows in Eq. (2).

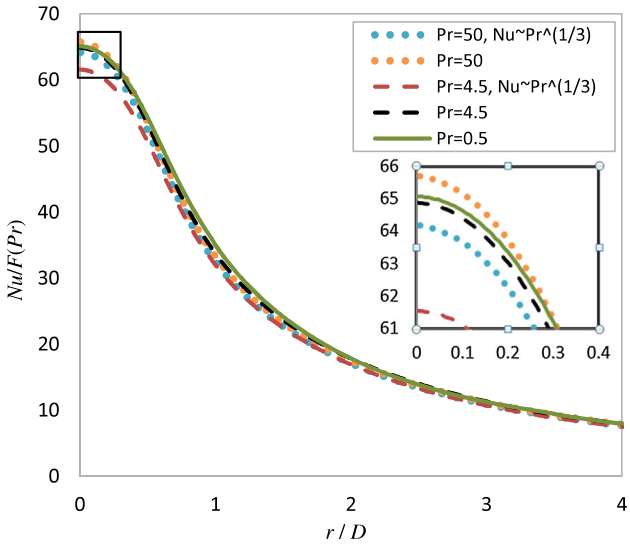

Fig. 12. Validation of heat transfer dependence on Prandtl number ($Nu \sim f(Pr)$ at $Re = 500$: $f(Pr) = G(Pr)$ given by Eq. (2) vs. $f(Pr) = 0.60105 \cdot Pr^{1/3}$.

The present curve features the well-known off-center heat transfer peak at $r/D \approx 0.5$, typical for partially developed issuing profiles [47,19,53]. Fig. 13b shows good agreement of the current local Nu distribution for water, similarly normalized, for the fully developed case at $Re = 500$ and 2000 with previous numerical data for air at and 1804 [3]. Fig. 13c presents a comparison of the current local Nu for the fully developed case at $Re = 500$ with experimental results at similar Re obtained with Ethylene Glycol and transformer oil [30], where Nu is normalized by Re and Pr to powers suggested by those authors. As Fig. 13c shows the agreement at the stagnation point is only reasonable, in part as the flow may still be approaching fully developed conditions ($L/D = 35$). It is also known that extrema values, such as occur at the stagnation point suffer from measurement limitations. For instance, with the method used there [30] peak values can be reduced by thermocouple leads conduction, resolution and accuracy, as well as thermal conduction in the heated foil which counters the high gradients found at the stagnation point. This possibility is further supported by the large dispersion in those results (see their Fig. 4), and empirically found Re dependence, $Nu \sim Re^{0.476}$, which deviates from laminar theory and present simulation results (see $Re = 2000$ curve in Fig. 13c).

With the simulations validated against previous studies, the simulated heat transfer distribution is examined more closely. Fig. 14 shows distributions of Nu for various L/D spanning almost two-orders of magnitude. The figure shows a distinct peak near $r/D = 0.5$ in the cases of the finite nozzle lengths examined, and a monotonous curve for the fully developed case. Starting from the shortest nozzle ($L/D = 0.25$), a clear trend of decreasing heat transfer is apparent until $L/D = 2$. This trend is in agreement with the trend of decreasing centerline velocity at low nozzle lengths that was found in the previous subsection (see Fig. 9b). However, a trend reversal occurs around $L/D = 3$, and heat transfer begins to increase with further increase in nozzle length, again in agreement with the trend of the maximal centreline velocity showed. Fig. 14c depicts the change in location of the peak Nu as a function of nozzle length, which is remains almost stationary up to $L/D = 2$ and gradually decreases thereafter.

These trends are presented in more detail in Fig. 15, where stagnation point Nu is plotted vs nozzle length for all Re and both Pr. All Nu curves feature a minimum around $Z = 0.0015$, corresponding to the flight velocity curves. Fig. 15 also shows a previous prediction

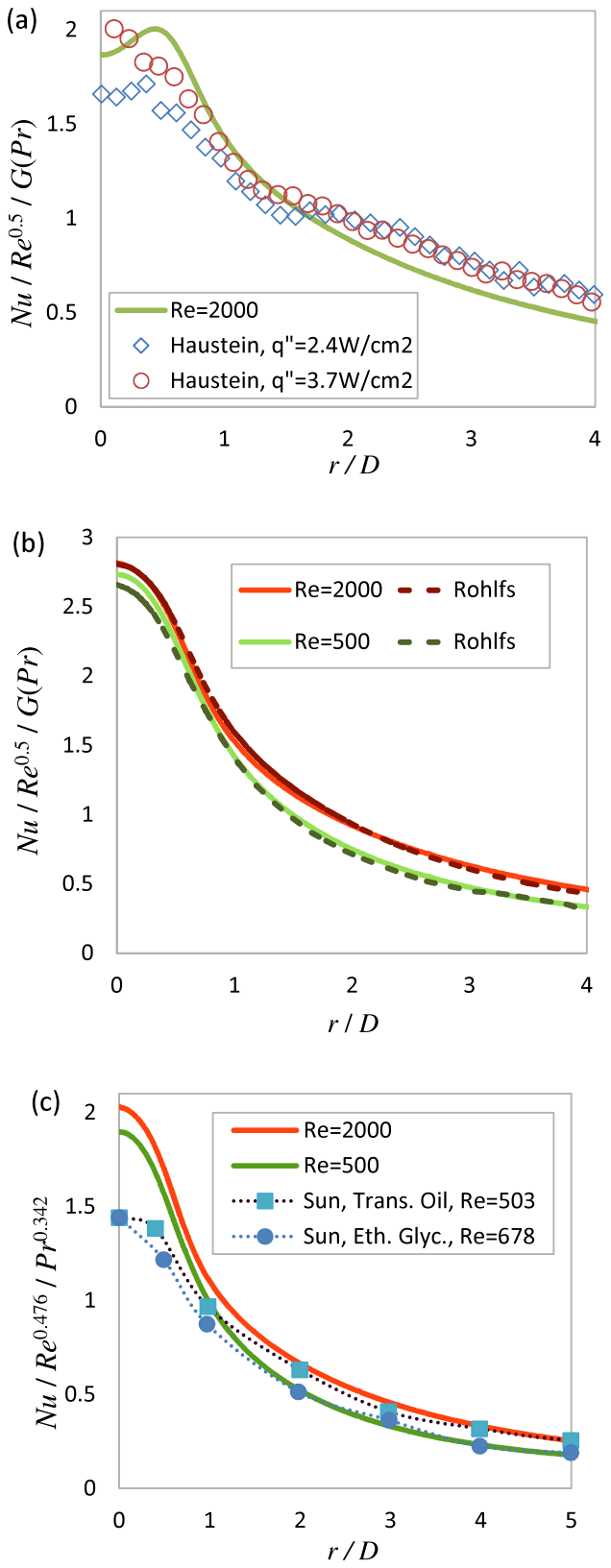

Fig. 13. Local Nu at $Re = 500$ and $Re = 2000$ for the fully developed case: (a) comparison to experimental results of [44], (b) comparison to the numerical results of [3], and (c) comparison to the experimental results of [30].

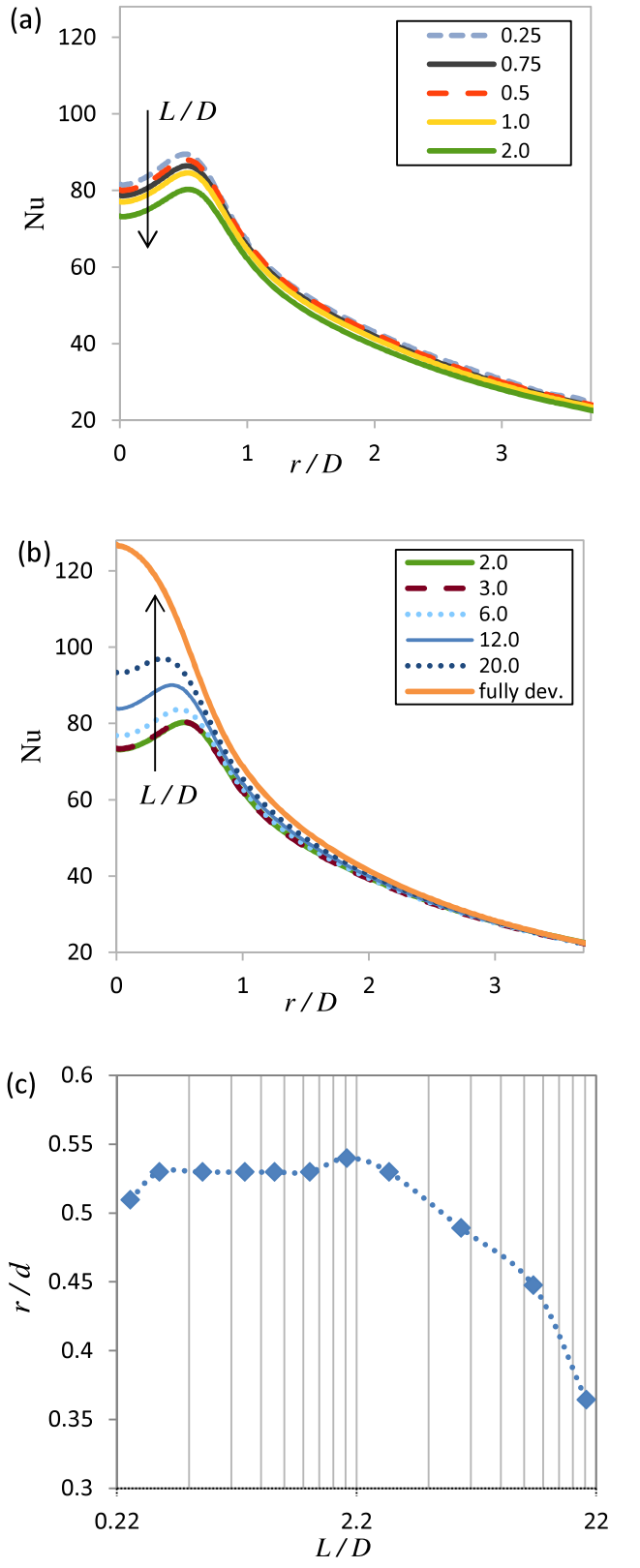

Fig. 14. Local Nu curves at $Re = 2000$: (a) up to L/D = 2, featuring off-center peak Nu that decreases with growing nozzle length for partially developed issuing profiles; (b) L/D = 2 and greater where the peak Nu increases with growing nozzle length, and a monotonous curve for the fully developed flow; and (c) the radial position of the off-center peak as a function of nozzle length.

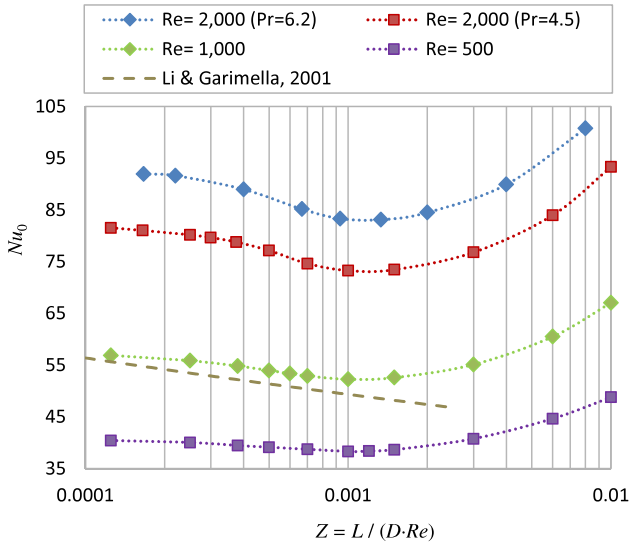

Fig. 15. Dependence of heat transfer coefficient at the stagnation point on the normalized nozzle length for all *Re* and *Pr* with comparison to a correlation for Nu_0 with dependence on L/D [11].

of stagnation point *Nu* as a function of nozzle length [11], given in Eq. (4) – developed for turbulent flows and here extrapolated beyond its range of validity, $Re > 4000$. Although the current results differ quantitatively from the predicted curve, the trend supports present results for short nozzle lengths, up to $Z = 0.001$.

As shown in this work, heat transfer depends on centerline velocity, which in turn depends on nozzle length. However, centerline velocity evolves during jet flight and therefore depends also on the nozzle-to-heater spacing, previously analyzed in [4]. Fig. 16 plots the resulting stagnation point heat transfer under a jet, subject to these effects. As the figure shows, three distinct branches can be identified – related to differing flow conditions: (i) short nozzle lengths within the peak *convergence* or *divergence* regimes; (ii) intermediate nozzle lengths within the pipe-flow *development* regime; (iii) fully developed issuing profile, undergoing relaxation during flight [4]. Herein, branches (i) and (ii) were found under conditions of short nozzle-to-heater spacing ($H = 3D$), so that the centerline velocity decreases very little prior to impingement.

It is of practical interest to adapt the previous model for centerline velocity to one for stagnation point heat transfer, in a straightforward manner.

3.4. Correlation for heat transfer

The trends of Nu_0 resulting from variation in nozzle length and depicted in Fig. 16 (branches i and ii) are simply expressed as a function of normalized centerline velocity, in a linear manner and similarly to [4] in Eq. (10). This equation involves three new constants denoted c_1 to c_3, which are found in the following.

$$Nu_0(\mathrm{U}) = \begin{cases} \mathrm{c}_1 + \mathrm{c}_2(\mathrm{U} - \mathrm{U}^*), & Z \leqslant Z^* \\ \mathrm{c}_1 + \mathrm{c}_3(\mathrm{U} - \mathrm{U}^*), & Z > Z^* \end{cases} \tag{10}$$

These constants must satisfy the following two constraints: at $U = 2$, i.e. the fully developed issuing profile, the development trendline coincides with the trendline for variation in H/D [4], namely reaching $Nu(U = 2) = 2.82$; and at $U = 1$ the same trendline, when extrapolated, receives the value of $Nu(U = 1) = 1.24$ for $Pr > 3$, derived from previous results for uniform issuing profile of a free-surface jet [45] according to Eq. (11). While the presents study deals with a submerged jet, the resulting heat transfer from both is very similar at short nozzle-to-heater spacing, as claimed previously by [46], and supported by previous results [4].

$$\frac{Nu}{\mathrm{G}(Pr)Re^{1/2}} = \frac{0.745 \cdot Re^{1/2}Pr^{1/3}}{\mathrm{G}(Pr)Re^{1/2}} \tag{11}$$

Finally, at U^{**} the value of $Nu(U^{**}) = Nu^{**} = 1.96$ was chosen as best fit to the current data, resulting in values for c_1 to c_3 of 1.783, 0.598 and 1.58, respectively.

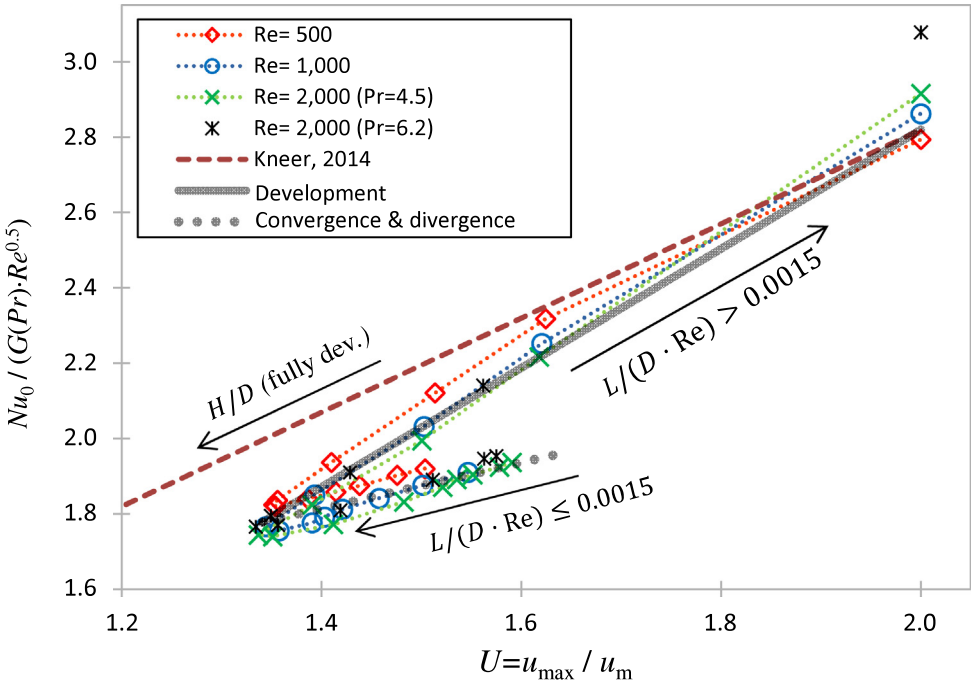

Fig. 16. Dependence of heat transfer coefficient at the stagnation point on the normalized centerline velocity featuring three distinct trends: two corresponding to variation in nozzle length and one corresponding to nozzle to heater distance, H/D, for fully developed issuing profile [4].

Substituting Eqs. (7) and (8) into Eq. (10) with all the values for the constants mentioned in the previous sections, we arrive at a correlation for heat transfer at the stagnation point dependent on *Pr*, *Re* and *Z*:

$$Nu_0 = G(Pr)\cdot Re^{1/2} \cdot \begin{cases} c_1 + c_2\left(\frac{1}{2}(U^{**}-U^{*}) - \frac{1}{2}(U^{**}-U^{*})\tanh(\zeta_2 \ln(Z/Z_{infl}))\right), & Z \leqslant Z^{*} \\ c_1 + c_2(2 - 1.18e^{-\zeta_1(Z+Z^{*})}), & Z > Z^{*} \end{cases} \quad (12)$$

The new correlation for stagnation point heat transfer captures the current data with a coefficient of determination, $R^2 = 0.966$ for the points within the valid range, and $R^2 = 0.963$ for all data points (Fig. 17). Overall, the models developed here for jet centerline velocity and stagnation-point heat transfer are quite simple and contain only 4 free parameters (Z^{*}, Z_{infl}, ζ_2 and Nu^{**}).

4. Discussion

In this work the influence of nozzle length in submerged jet impingement heat transfer was studied numerically. The conditions examined here were chosen so as to minimize additional effects on the impingement centerline velocity, thereby the study

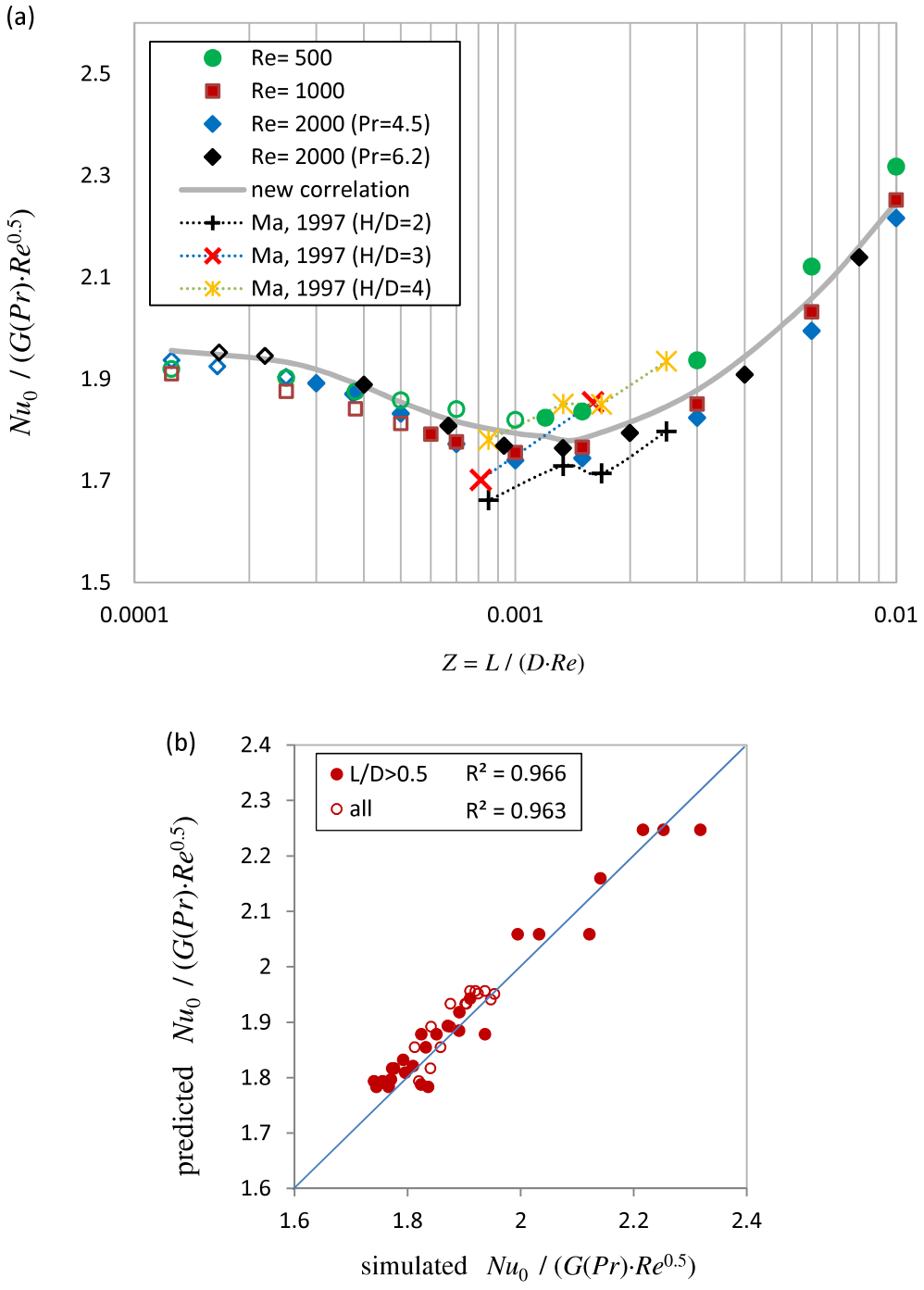

Fig. 17. Evaluation of heat transfer prediction by the new model: (a) Prediction by Eq. (12). (b) Evaluation of prediction performance within the valid range ($L/D > 0.5$) and for all data point.

was limited to a low nozzle-to-heater spacing ($H/D = 3$) and ideal, undisturbed inlet conditions. This parameter was not varied as together with the nozzle length variation examined here this would create a high level of complexity beyond the scope of this study. Moreover, some previous studies have already dealt with its influence on heat transfer (see e.g. [1] for a list of experimental correlations involving H/D – there termed z/d; or Kneer et al. [4], for the dependence in the case of a fully developed profile). Therein, axisymmetric transient, direct numerical simulations were validated against experimental and numerical literature. The current numerical parametric study provided a new detailed characterization of short nozzle's flow regimes, leading to a physics-based correlation for the characteristic jet centerline velocity and the resulting stagnation-point heat transfer.

It was shown here for $Re = 500$, 1000 and 2000 that impingement heat transfer depends strongly on the centerline velocity, which in turn, depends on nozzle length. Centerline velocity at the nozzle exit plane vs nozzle length was found to be non-monotonous with one local maximum that varies with *Re*, and one local minimum at $Z \approx 0.0015$ for all *Re* considered (see Fig. 9a). For a nozzle with a sharp-edged inlet, in terms of maximal centerline velocity attained, also reflected in the heat transfer, three physical regimes were identified. These are, in order of increasing length: (i) at very short lengths (up to $L/D \leqslant 0.6$) the *convergence* regime is encountered, wherein the flow is converging inside the nozzle; (ii) above these lengths ($0.6 \leqslant L/D$ and $L/(D \cdot Re) \leqslant 0.0015$) the flow diverges within the nozzle and centerline reduces – a range termed the *divergence* regime (relating to the separation bubble); (iii) Once the flow is fully reattached ($0.0015 \leqslant L/(D \cdot Re)$) the centerline begins to accelerate with increase in nozzle length, similarly to nominal pipe flow – termed the *development* regime.

In the *convergence* regime the velocity profile seen at the nozzle exit-plane is not yet at its final form, obtained at the vena-contracta - the location of maximal contraction, and is therefore characterized by an off-center velocity peak. This peak disappears, following the extra-nozzle acceleration of the centerline. Plotting the centerline velocity revealed that in the *convergence* regime, it does not scale with $L/(D \cdot Re)$ and is difficult to predict without introducing a new scaling. While in the other two regimes centerline velocity scales directly with $L/(D \cdot Re)$ and a predictive model has been developed.

The centerline velocity correlation developed here (Eqs. (7) and (8)) is valid for the *divergence* and *development* regimes, which corresponds to a validity range of $L/D \geqslant 0.6$ and $500 \leqslant Re \leqslant 2000$. Within this range successful prediction is obtained ($R^2 = 0.98$) of present simulations for water flow at two different Prandtl numbers and covering a very wide range of nozzle lengths. By relying on previous findings this empirical correlation requires only three free parameters – one of which is the transition point between these two regimes and their opposing trends. The identified regimes are clearly represented in the resulting stagnation point heat transfer, shown in Fig. 15, where two distinct linear relations to centerline velocity (two straight branches) are seen, differing from a third linear relation found previously for jet time-of-flight [4]. Based on these linear relations the velocity correlation developed is converted into a new heat transfer correlation. This new heat transfer correlation (Eq. (12)) adds one additional free parameter – the maximal stagnation heat transfer at infinitesimally short nozzles. Due to the reliance of the heat transfer correlation on the velocity one, the stated ranges of validity are identical, and quite good agreement is found with present simulations ($R^2 = 0.97$), experimental results from the literature for much more viscous transformer oil [47], and a short-nozzle trend found at much higher *Re* [11]. This correlation provides a design tool for practical applications, especially at the micro-scale where constraints correspond with the present model's validity range.

Through these insights and correlations the present study lays a foundation for dealing with the heat transfer and flow of partially developed jets, even below $L/D = 1$. Due to the adherence to the full Navier-Stokes method without any turbulence modeling, flows were limited to $Re \leqslant 2000$, though the relations and trends found may well extend to higher *Re*. Although the present simulations were conducted for a *single-jet*, the findings are also relevant to the more commonly used configuration of jet arrays. This is exemplified in the foundational work of Martin [48], who developed a correlation for arrays founded on the case of a single jet. This similarity to arrays is further supported by the high level of axisymmetry observed in small arrays or in arrays with inter-jet fluid extraction, where crossflow effects are significantly reduced [49].

As the present model was developed from idealized flows without the occurrence of significant vortices in the simulations (quasi-steady conditions), some deviation from findings may be expected under disturbed conditions, typical to higher *Re* flows. Recently, it has been demonstrated that with great care these conditions can be experimentally reproduced even at high *Re* [50], and that even the occurrence of these *instantaneous* vortices has little effect on the time-averaged velocity and resulting heat transfer [3].

Conflict of interest

The study titled "Dependence of Submerged Jet Heat Transfer on Nozzle Length" is a numerical fundamental work, and therefore there are no foreseeable conflict of interests involved with this article.

Acknowledgement

This work was supported by the Israel Science Foundation [grant number 4112/17].

References

[1] C.F. Ma, Y.P. Gan, Y.C. Tian, D.H. Lei, T. Gomi, Liquid jet impingement heat transfer with or without boiling, J. Therm. Sci. 2 (1993) 32–49.
[2] N. Zuckerman, N. Lior, Jet impingement heat transfer: physics, correlations, and numerical modeling, Adv. Heat Transf. 39 (2006) 565–631.
[3] W. Rohlfs, H.D. Haustein, O. Garbrecht, R. Kneer, Insights into the local heat transfer of a submerged impinging jet: influence of local flow acceleration and vortex-wall interaction, Int. J. Heat Mass Transf. 55 (2012) 7728–7736.
[4] R. Kneer, H. D. Haustein, C. Ehrenpreis, W. Rohlfs, Flow structures and heat transfer in submerged and free laminar jets, in: 15th Internation Heat Transfer Conference (IHTC-15), 2014, p. 15.
[5] P. Gulati, V. Katti, S.V. Prabhu, Influence of the shape of the nozzle on local heat transfer distribution between smooth flat surface and impinging air jet, Int. J. Therm. Sci. 48 (2009) 602–617.
[6] J. Lee, S.-J. Lee, The effect of nozzle aspect ratio on stagnation region heat transfer characteristics of elliptic impinging jet, Int. J. Heat Mass Transf. 43 (2000) 555–575.
[7] C.H. Amon, S.-C. Yao, C.-F. Wu, C.-C. Hsieh, Microelectromechanical system-based evaporative thermal management of high heat flux electronics, J. Heat Transf. 127 (2005) 66–75.
[8] L.A. Brignoni, S.V. Garimella, Effects of nozzle-inlet chamfering on pressure drop and heat transfer in confined air jet impingement, Int. J. Heat Mass Transf. 43 (2000) 1133–1139.
[9] A. Royne, C.J. Dey, Effect of nozzle geometry on pressure drop and heat transfer in submerged jet arrays, Int. J. Heat Mass Transf. 49 (2006) 800–804.
[10] B.P. Whelan, A.J. Robinson, Nozzle geometry effects in liquid jet array impingement, Appl. Therm. Eng. 29 (2009) 2211–2221.
[11] C.-Y. Li, S.V. Garimella, Prandtl-number effects and generalized correlations for confined and submerged jet impingement, Int. J. Heat Mass Transf. 44 (2001) 3471–3480.
[12] A.J. Ward-Smith, Critical flowmetering: the characteristics of cylindrical nozzles with sharp upstream edges, Int. J. Heat Fluid Flow 1 (1979) 123–132.
[13] H.L. Langhaar, Steady flow in the transition length of a straight tube, J. Appl. Mech 9 (1942) 55–58.
[14] K. Garrett, B.W. Webb, The effect of drainage configuration on heat transfer under an impinging liquid jet array, J. Heat Transf. 121 (1999) 803–810.

[15] D.-H. Rhee, P.-H. Yoon, H.H. Cho, Local heat/mass transfer and flow characteristics of array impinging jets with effusion holes ejecting spent air, Int. J. Heat Mass Transf. 46 (2003) 1049–1061.
[16] C. Meola, G.M. Carlomagno, Intensive cooling of large surfaces with arrays of jets, in: Proceedings of QIRT, 2006.
[17] A. Royne, C.J. Dey, Design of a jet impingement cooling device for densely packed PV cells under high concentration, Solar Energy 81 (2007) 1014–1024.
[18] A.J. Robinson, E. Schnitzler, An experimental investigation of free and submerged miniature liquid jet array impingement heat transfer, Exp. Therm Fluid Sci. 32 (2007) 1–13.
[19] A.M. Huber, R. Viskanta, Convective heat transfer to a confined impinging array of air jets with spent air exits, J. Heat Transf. 116 (1994) 570–576.
[20] E.N. Wang, L. Zhang, L. Jiang, J.-M. Koo, J.G. Maveety, E.A. Sanchez, K.E. Goodson, T.W. Kenny, Micromachined jets for liquid impingement cooling of VLSI chips, J. Microelectromech. Syst. 13 (2004) 833–842.
[21] T. Brunschwiler, H. Rothuizen, M. Fabbri, U. Kloter, B. Michel, R.J. Bezama, G. Natarajan, Direct liquid jet-impingment cooling with micron-sized nozzle array and distributed return architecture, in: The Tenth Intersociety Conference on Thermal and Thermomechanical Phenomena in Electronics Systems, 2006, ITHERM'06, 2006, pp. 196–203.
[22] E.A. Browne, G.J. Michna, M.K. Jensen, Y. Peles, Experimental investigation of single-phase microjet array heat transfer, J. Heat Transf. 132 (2010) 041013.
[23] A. Bhunia, C.L. Chen, On the scalability of liquid microjet array impingement cooling for large area systems, J. Heat Transf. 133 (2011) 064501.
[24] G. Natarajan, R.J. Bezama, Microjet cooler with distributed returns, Heat Transf. Eng. 28 (2007) 779–787.
[25] Y. Won, E.N. Wang, K.E. Goodson, T.W. Kenny, 3-D visualization of flow in microscale jet impingement systems, Int. J. Therm. Sci. 50 (2011) 325–331.
[26] B. Elison, B.W. Webb, Local heat transfer to impinging liquid jets in the initially laminar, transitional, and turbulent regimes, Int. J. Heat Mass Transf. 37 (1994) 1207–1216.
[27] A.C. Cotler, E.R. Brown, V. Dhir, M.C. Shaw, Chip-level spray cooling of an LD-MOSFET RF power amplifier, IEEE Trans. Compon. Packag. Technol. 27 (2004) 411–416.
[28] W. Rohlfs, M. Bieber, C. Ehrenpreis, J. Jörg, E. Sabelberg, R. Kneer, Flow structures and heat transfer characteristics in arrays of submerged laminar impinging jets, PAMM 16 (2016) 953–956.
[29] F.M. White, Viscous Fluid Flow, McGraw-Hill, New York, 1974.
[30] H. Sun, C.F. Ma, Y.Q. Tian, Local convective heat transfer from small heaters to impinging submerged axisymmetric jets of seven coolants with Prandtl number ranging from 0.7 to 348, J. Therm. Sci. 6 (1997) 286–297.
[31] C. Meola, A new correlation of Nusselt number for impinging jets, Heat Transf. Eng. 30 (2009) 221–228.
[32] G.W. Hall, Analytical determination of the discharge characteristics of cylindrical-tube orifices, J. Mech. Eng. Sci. 5 (1963) 91–97.
[33] T.A. Jankowski, E.N. Schmierer, F.C. Prenger, S.P. Ashworth, A series pressure drop representation for flow through orifice tubes, J. Fluids Eng. 130 (2008) 051204.
[34] M. Fabbri, V.K. Dhir, Optimized heat transfer for high power electronic cooling using arrays of microjets, J. Heat Transf. 127 (2005) 760–769.
[35] B. Kashi, H.D. Haustein, The importance of nozzle length and issuing profile in submerged impinging jet heat transfer, in: Proceedings of CHT-17 ICHMT International Symposium on Advances in Computational Heat Transfer, Napoli, Italy, 2017, pp. 501–510.
[36] P.J. Roache, A method for uniform reporting of grid refinement studies, ASME-Publications-FED 158 (1993) 109, 109-109.
[37] I.B. Celik, U. Ghia, P.J. Roache, et al., Procedure for estimation and reporting of uncertainty due to discretization in CFD applications, J. Fluid Eng-T. ASME 130 (2008) 078001–1/4.
[38] B.S. Massey, J. Ward-Smith, Mechanics of Fluids, CRC Press, 1998.
[39] F. Durst, S. Ray, B. Ünsal, O.A. Bayoumi, The development lengths of laminar pipe and channel flows, J. Fluids Eng. 127 (2005) 1154.
[40] H.D. Haustein, R.S. Harnik, W. Rohlfs, A simple hydrodynamic model of a laminar free-surface jet in horizontal or vertical flight, Phys. Fluids 29 (2017) 082105.
[41] J.H. Lienhard, Velocity coefficients for free jets from sharp-edged orifices, J. Fluids Eng. 106 (1984) 13–17.
[42] F.C. Johansen, Flow through pipe orifices at low Reynolds numbers, Proc. R. Soc. Lond. Ser. A, Contain. Papers Math. Phys. Charact. 126 (1930) 231–245.
[43] D. Wu, R. Burton, G. Schoenau, An empirical discharge coefficient model for orifice flow, Int. J. Fluid Power 3 (2002) 13–19.
[44] H.D. Haustein, G. Tebrügge, W. Rohlfs, R. Kneer, Local heat transfer coefficient measurement through a visibly-transparent heater under jet-impingement cooling, Int. J. Heat Mass Transf. 55 (2012) 6410–6424.
[45] X. Liu, J.H. Lienhard, J.S. Lombara, Convective heat transfer by impingement of circular liquid jets, J. Heat Transf. 113 (1991) 571–582.
[46] J. Lienhard, Liquid jet impingement, Ann. Rev. Heat Transf. 6 (1995).
[47] C.F. Ma, Q. Zheng, S.C. Lee, T. Gomi, Impingement heat transfer and recovery effect with submerged jets of large Prandtl number liquid—I. Unconfined circular jets, Int. J. Heat Mass Transf. 40 (1997) 1481–1490.
[48] H. Martin, Heat and mass transfer between impinging gas jets and solid surfaces, Adv. Heat Transf. 13 (1977) 1–60.
[49] A.M. Huber, R. Viskanta, Comparison of convective heat transfer to perimeter and center jets in a confined, impinging array of axisymmetric air jets, Int. J. Heat Mass Transf. 37 (1994) 3025–3030.
[50] W. Rohlfs, J. Jörg, C. Ehrenpreis, M. Rietz, H. Haustein, R. Kneer, Flow structures and heat transfer in submerged laminar jet impingement. In: Proceedings of the 1st Thermal and Fluids Engineering Summer Conference, TFESC-1, 2015, New York, USA paper TFESC-12816.
[51] http://www.openfoam.org, 2017.
[52] W. Rohlfs, C. Ehrenpreis, H.D. Haustein, R. Kneer, Influence of viscous flow relaxation time on self-similarity in free-surface jet impingement, Int. J. Heat Mass Transf. 78 (2014) 435–446.
[53] M. Angioletti, R.D. Tommaso, E. Nino, G. Ruocco, Simultaneous visualization of flow field and evaluation of local heat transfer by transitional impinging jets, Int. J. Heat Mass Transf. 46 (10) (2003) 1703–1713.